IOSR Journal Of Applied Physics (IOSR-JAP)
e-ISSN: 2278-4861.Volume 15, Issue 6 Ser. I (Nov. – Dec. 2023), PP 24-31
www.Iosrjournals.Org

Structural, Morphological And Optical Properties Of Cerium Doped $Znal_2o_4$

K. Kiran Kumar[1], T. Suresh Kumar[1], G.Sriramulu[1], S. Katlakunta[1*]
[1]*Department of Physics, University College of Science, Saifabad, Osmania University, Hyderabad, India.*

Abstract
A series of $ZnAl_{2-y}Ce_yO_4$ (y = 0.0 - 0.10) ceramics were prepared by using microwave-hydrothermal method at 200°C /60 min. The ceramic powders were conventionally sintered at 1250°C/4 h. All of the samples have a cubic crystal structure and belong to the space group Fd-3m. The lattice constant (a) linearly increased from 8.085 Å (y = 0.0) to 8.404Å (y = 0.10).The average crystallite size (<D>) in the range of 61 – 90 nm. The FESEM images show irregular morphology and non-distribution of grains.The Fourier transform infrared spectra (FTIR) shows tetrahedral and octahedral absorption bands in the region, 411 - 431 cm^{-1} and 497 – 649 cm^{-1}, respectively. The UV-vis spectra shows that the bandgap energy (E_g) value is decreased from 3.51 eV (y = 0.0) to 4.11 eV (y = 0.10) with Ce^{3+} doping. The X-ray photoelectron spectroscopy confirmed the valence states of Zn, Al, Ce and O.
Keywords: *Nanoparticles, microwave- hydrothermal method, X-ray diffraction, XPS, Energy band gap,*

Date of Submission: 18-11-2023 Date of Acceptance: 28-11-2023

I. Introduction

Zinc aluminate ($ZnAl_2O_4$) is a member of the spinel family with the general formula AB_2O_4. This material has wide range of applications in optical and ceramic industries [1, 2]. With an optical band gap of 3.8-3.9 eV, this compound is reported to be transparent and electro conductive as result of which it can be used for ultraviolet (UV) photoelectronic devices. Further, the material is also employed in various catalytic reactions such as cracking, dehydration, hydrogenation and dehydrogenation in chemical and petrochemical industries [3].

CeO_2 is a rare earth oxide has attracted much consideration in the middle of the researchers because of its extensive use in various fields such as photo catalysis, solid oxide fuel cells, glass polishing supplies, water gas shift and UV absorbents [4]. Due to its high oxygen storage capacity with rich oxygen vacancies and a capability to form a Ce^{3+}/Ce^{4+} red-ox pair because of high reduction potential, CeO_2 can serve as a very high-quality photo catalyst [5].

Over the past few years, Ce^{3+} ion has been widely investigated because of its emission and absorption spectra which consist of broad bands due to the transitions between the $4f_1$ ground state and the crystal field components of the 5d excited state configuration. In addition, the 5d state of Ce^{3+} is sensitive to the lattice environment and the emission spectrum location of Ce^{3+} could be adjusted from near blue to green, yellow, and even to orange [6, 7]. Among the broad variety of inorganic hosts, aluminates have attracted great attention in recent years and could be regarded as the Ce^{3+} doped lattice due to their low cost, high chemical stability, excellent weather resistance and variety of crystal structure [8].

There have been a number of rare earth metal ions and transition metal ions used as the dopants. The Ce^{3+} has seen extensive used as a dopant for the $ZnAl_2O_4$ host material because of the close proximity in ionic radii that it shares with rare earth ions [9]. Different synthesis were employed to prepare $ZnAl_2O_4$ such as solid state method [10, 11], hydrothermal synthesis [12, 13], sol-gel method [14, 15]. The solid state synthesis needs the physical mixing of the various precursors, followed by sintering [16]. It also require high temperature sintering and long hours. It is difficult to control the particle size and maintain the homogeneity [17]. The chemical methods are advantageous due to easy preparation methods, high yields, requires low sintering temperatures and time, homogeneity etc. Among these microwave hydrothermal synthesis method offers low synthesis temperature, novel phases, saves energy and time, high yield [18, 19].

Therefore, in the present investigation, the microwave-hydrothermal method is used for the synthesis of Ce doped $ZnAl_2O_4$ nanoparticles. The influence of Ce^{3+} on the structural, spectroscopic and optical properties were studied using X-ray diffraction (XRD), Fourier transform Infrared spectroscopy (FTIR), UV-Vis spectrometer, and X-ray photoelectron spectroscopy (XPS) and all the results are explained in detail.

II. Experimental method

For the synthesis, analytical grade chemicals $Zn(NO_3)_2.6H_2O$, $Al(NO_3)_3.9H_2O$ and $Ce(NO_3).6H_2O$ of 99.98% purity were used. The synthesis of $ZnAl_{2-y}Ce_yO_4$ (y = 0.00 - 0.10 in steps of 0.02) nanopowders were synthesized using microwave-hydrothermal method. The powders were weighed and then dissolved in deionized water. To get a pH of 11, NaOH was slowly added to the clear solution. The microwave accelerated reaction system (MARS-5, CEM Corp., Mathews, NC) was used to treat the precipitate at 200°C for 60 minutes. It runs at a frequency of 2.45 GHz and a power of 1200±50W. The product was properly filtered and washed with deionized water until the pH was neutral. The powders were then dried overnight at 80° in an oven. The dried powders were finally sintered at 1250°C for 4 hours in a muffle furnace.

The X-ray diffraction patterns were recorded for the sintered samples using an X-ray diffractometer (Phillips PANanalytical) with Cu-K irradiation (1.5406 Å) in the scanning range of 2θ = 20°–80° with a scan rate of 1°/min at 40 kV and 30 mA. The morphology studies were carried out using a field emission scanning electron microscope (FE-SEM). The Fourier transform infrared (FTIR) spectrum was recorded on the Brucker-Tensor 27 spectrometer in the mid-IR range of 4000–400 cm^{-1} with a resolution of 4 cm^{-1}. The samples were prepared using the KBr pellet method. The absorbance spectra were recorded on a UV-visible spectrophotometer (Shimadzu, UV-1800) over a scanning range of 200–900 nm at a resolution of 1 nm. XPS measurements were made on a Shimadzu ESCA-3400 spectrophotometer (Kyoto, Japan) using a monochromatic Mg-K X-ray source (1253.6 eV) operating at 10 kV and 10 mA.

III. Results and Discussion

X-ray diffraction analysis (XRD)

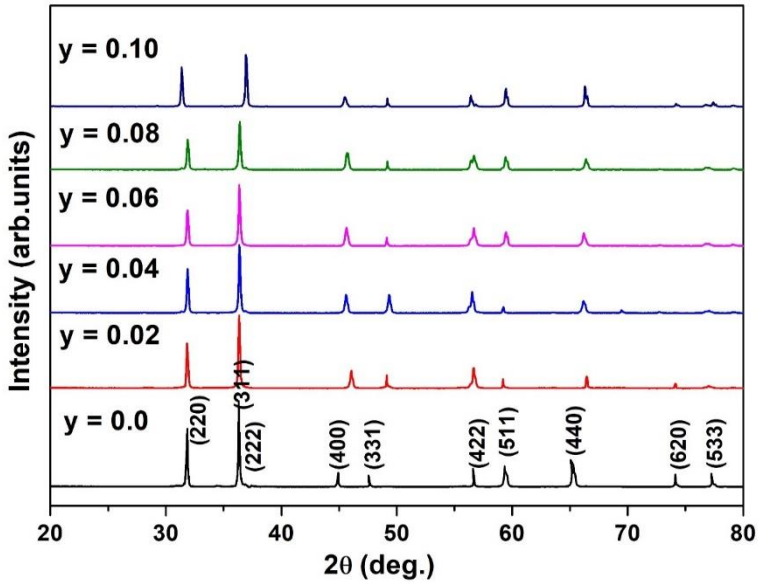

Fig. 1 X-ray diffraction patterns of $ZnAl_{2-y}Ce_yO_4$ (y = 0.0 – 0.10).

To study the crystalline structure and calculate the lattice parameters of the Ce^{3+} doped $ZnAl_2O_4$, XRD technique was used. The recorded XRD patterns in the range of 20 - 80° are depicted in Fig. 1. The XRD pattern of sintered $ZnAl_2O_4$:Ce^{3+} matched with the standard patterns of cubic $ZnAl_2O_4$ spinel (JCPDS file No 74-1138) belong to Fd-3m space group (227). All the samples exhibit major diffraction peaks. These peaks can be indexed as (220), (311), (222), (400), (331), (422), (511), (440), (620) and (533) diffractions. It was noticed that the introduction of Ce does not create any other phases in samples. It was noticed that as the Ce^{3+} content increases, the diffraction peak at 2θ = 36.758 (311) exhibits the most noticeable change with its decreased intensity. Further, it was observed that the position of the main diffraction peaks (311) of $ZnAl_2O_4$:Ce^{3+} samples slightly shifted towards lower angle side with increasing Ce^{3+} concentration (Fig.1), which indicating increased inter planar spacing. However, there is no systematic movement in the position of reflection peaks observed.

The lattice constant (a), X-ray density (d_x), and volume of the unit cell (V), were calculated by using equations (1) – (3) [20 - 22],

$$a = d\sqrt{h^2 + k^2 + l^2}\ \text{Å} \quad \text{……(1)}$$

$$V = a^3\ \text{Å}^3 \quad \text{……..(2)}$$

$$d_x = \frac{8M}{N_A a^3}\ \text{g/cm}^3 \quad \text{……...(3)}$$

where d is interplanar distance, M is the molecular weight of the sample, N_A is Avagadro's number, and h,k,l are miller indices. The bulk density (d_b) of all the samples are calculated using Archimedes principle. The average crystallite size (<D>) and lattice strain (ε) is calculated from Williamson-Hall plot as shown in Fig. 2. The lattice strain (ε) and crystallite size (<D>) is obtained from equation

$$\beta = \frac{k\lambda}{D\cos\theta} + 4\varepsilon \tan\theta \quad \ldots\ldots\ldots\ldots\ldots\ldots (4)$$

where β represents Full Width at Half Maxima (FWHM) of the diffraction peaks, θ is the diffraction angle in radians, λ is the wavelength of the X-rays, the constant k = 0.9. The calculated values for lattice strain (ε), crystallite size (<D>), lattice constant (a), volume of the unit cell (V), X-ray density (d_x), bulk density (d_b) and porosity (%P) are tabulated in Table 1. Fig.3 shows the variation of lattice constant (a) with Ce doping (y). It is observed that a is linearly increased from 8.085 Å (y = 0.0) to 8.144Å (y = 0.10). It shows that with Ce doped $ZnAl_2O_4$ sample does obey Vegard's law. The increase in lattice constant, a is due the substitution of smaller ionic radii of Al^{3+} (0.53 Å) by higher ionic radii, Ce^{3+} (1.143 Å) [23]. A similar variation is observed elsewhere [23]. The unit cell volume (V) follows similar variation as lattice constant indicates that the solubility of Ce^{3+} in $ZnAl_2O_4$ lattice. The linear variation of d_x with y is due to the difference in the molar mass of the Ce (140.12 g/mol), Al (27 g/mol) and Zn (65.4 g/mol). The bulk density (d_b) is varied non linearly with y. The percentage of porosity (%P) is in between 3 to ~8 %. The average crystallite size (<D>) is calculated from W-H plots and is found to be in the range of 61 – 90 nm. The increase in lattice strain (ε) is may be due to the creation of oxygen vacancies on the surface of nanoparticles [24].

Fig.2 Williamson-Hall plots for y = 0.0 - 0.10.

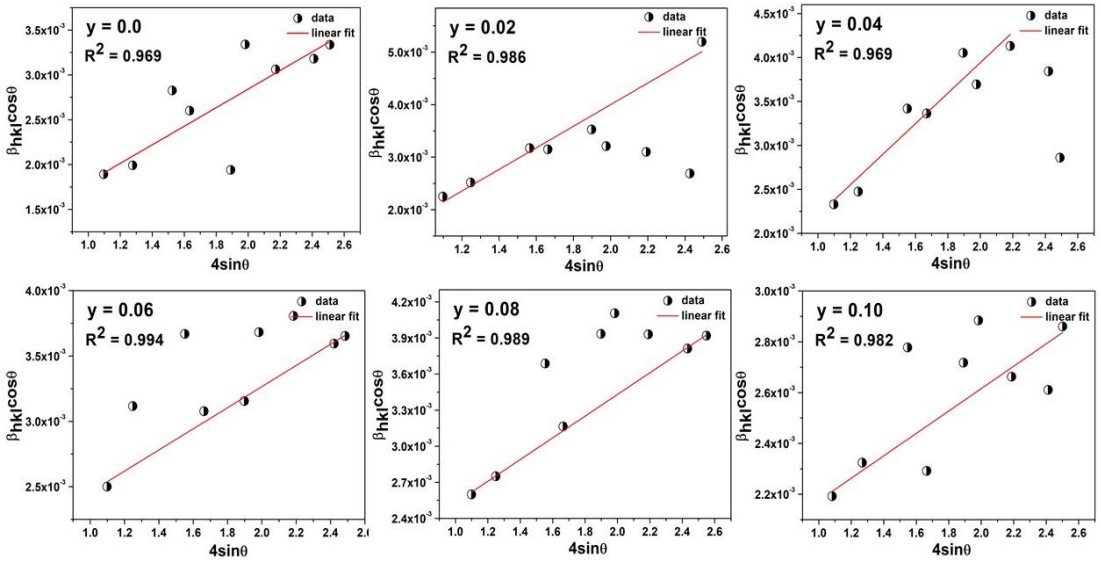

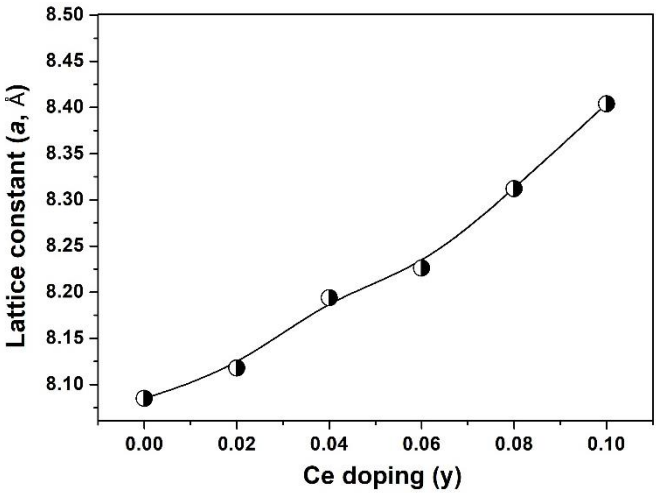

Fig. 3 Variation of lattice constant (a) with Ce doping (y).

Table 1 Structural parameters: lattice constant (*a*), unit cell volume (*V*), X-ray density (d_x), bulk density (d_b), percentage of porosity (%P), and crystallite size <D>.

y (mol %)	Lattice constant (*a*) (Å)	Volume (V) (Å^3)	X-ray density (d_x) (g/cm^3)	Bulk density (d_b) (g/cm^3)	Porosity (%P)	Crystallite size (<D>) (nm)	Strain ε x 10^{-3}
0.00	8.085	528.494	3.401	3.252	4	70	2.71
0.02	8.118	534.992	3.416	3.167	7	78	2.94
0.04	8.194	550.159	3.376	3.261	3	90	3.25
0.06	8.226	556.629	3.391	3.248	4	74	2.66
0.08	8.312	574.271	3.339	3.112	6	66	2.11
0.10	8.404	593.551	3.281	3.015	8	61	1.82

Field

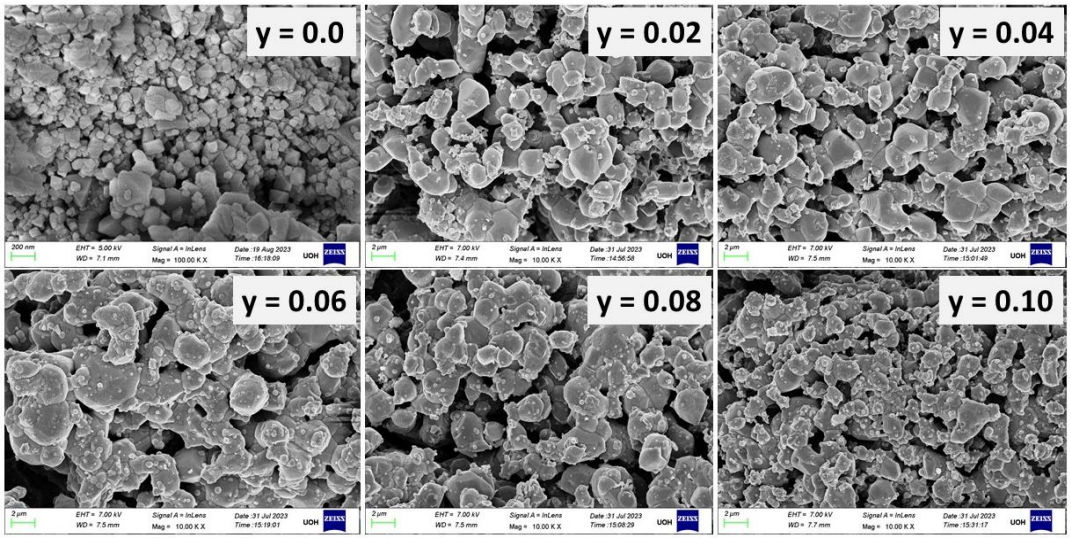

Fig.4 FESEM images for *y* = 0.0 – 0.10.

The morphology, grain size and energy dispersive spectra (EDS) of $ZnAl_{2-y}Ce_yO_4$ (y = 0.0 - 0.10) samples have been investigated using field emission scanning microscopy (FESEM). SEM images of the present investigated samples are shown in Fig.4. The images show irregular morphology and non-distribution of grains. Fig.5 represents the EDS spectrum of all the samples where the presence of Zn, Al, Ce, and O elements were confirmed, which indicates that there are no impurities present in the prepared samples. It is seen that all the elements have been uniformly distributed on the surface of the samples.

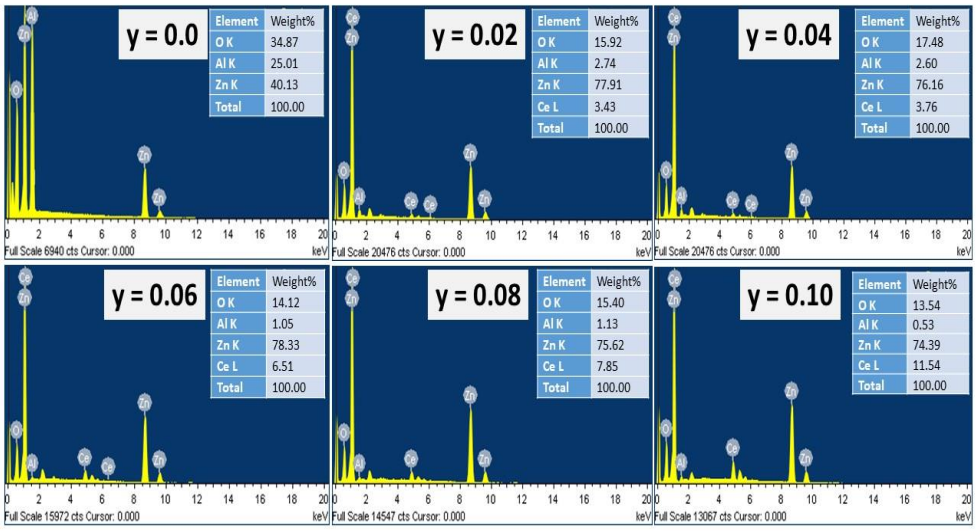

Fig.5 FESEM images for *y* = 0.0 – 0.10.

FTIR spectroscopy:

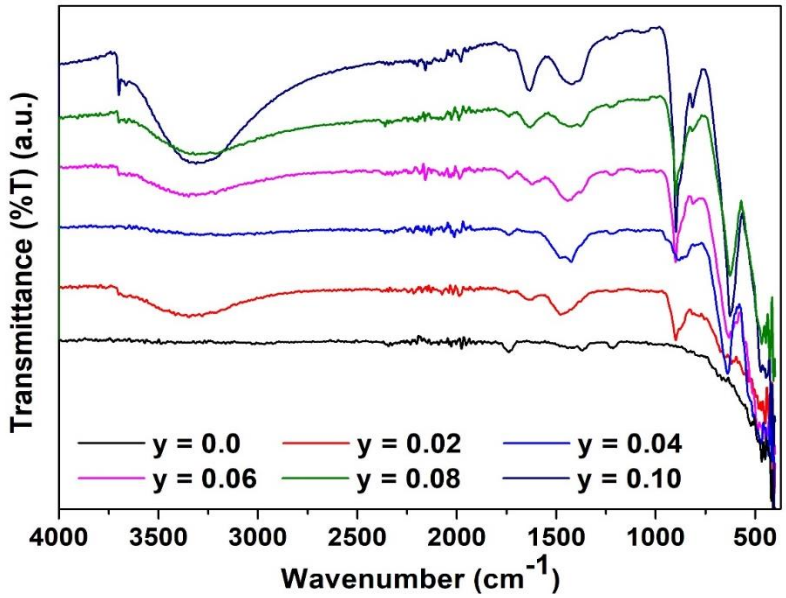

Fig.6 FTIR spectra of $ZnAl_{2-y}Ce_yO_4$ (y = 0.0 – 0.10).

The FTIR analysis was employed to evaluate the surface chemistry of sintered $ZnAl_{2-y}Ce_yO_4$ (y = 0.0 - 0.10) samples in the range of 400 – 4000 cm^{-1}, as shown in Fig.6. The absorption bands for samples y = 0.0 to 0.10 are tabulated in Table 2. Obviously, the broad and strong peaks at the wavenumbers of ~3311 - 3394 cm^{-1} and 1626 - 1639 cm^{-1} are related to the stretching vibration and bending vibration of hydroxyl groups of absorbed water [25, 26] for all the samples. Also, the NH bending vibrations appear at the wavenumber of 1412 to 1483 cm^{-1}. The absorption bands ~649 cm^{-1}, and 497 cm^{-1} for sample y = 0.0 corresponds to Zn-O and Al-O symmetric stretching vibrations [27, 28]. The presence of these peaks indicates the formation of spinel cubic phase. Compared to absorption bands 497 cm^{-1}, the intensity of 649 cm^{-1} is varied with doping, y. The change in intensity indicates that Ce^{3+} ions enter into the spinel lattice where it replaces Al^{3+} ions. The 411 cm^{-1} and 431 cm^{-1} bands are appeared due to the tetrahedral Al^{3+} [29 - 31].

Table 2. Structural bonds obtained from FTIR for y = 0.0 – 0.10.

y = 0.0 (cm^{-1})	y = 0.02 (cm^{-1})	y = 0.04 (cm^{-1})	y = 0.06 (cm^{-1})	y = 0.08 (cm^{-1})	y = 0.10 (cm^{-1})
411	417	416	416	410	411
431	428	427	525	429	432
497	**495**	**493**	**499**	**500**	**499**
649	**653**	**656**	**652**	**650**	**650**
809	895	894	900	900	903
1483	1473	1412	1425	1414	1420
1639	1629	1637	1626	1626	1632
---	3338	3394	3312	3311	3316

UV-Vis Spectroscopy:

Fig.7 (a) shows the UV-Vis absorbance spectra of $ZnAl_{2-y}Ce_yO_4$ (y = 0.00 - 0.10) nanoparticles recorded in the wavelength range 200 – 800 nm. The absorption edge in the lower wavelength region (230 - 279 nm) is due to the distortion of lattice by the Ce doping at Al^{3+} sites [32]. The absorbance is high around 330 nm for all the samples corresponds to visible range. It is reported that impurities in the sample, band gap energy, oxygen deficiency, and particle size may influence the absorbance in the sample [33]. The optical band gap for all the samples were calculated using the Tauc plots using the equation [34]

$$\alpha(\nu)h\nu = \left(h\nu - E_g\right)^n$$

where E_g is the band gap energy, $h\nu$ is the incident photon energy, $\alpha(\nu)$ is absorption coefficient, ν is the frequency of vibration and n = ½ for direct band gap semiconductors. An extrapolation of the linear region of the plot of $h\nu$ vs $(\alpha h\nu)^2$ gives the value of the optical band gap E_g. The two absorption bands in the range of 320 - 375

nm, and 580 - 700 nm were observed for all the samples. The absorption bands in between 320 - 375 nm is may be due to the transitions from O-Al in tetrahedral sites. The transitions involving O-Al in octahedral sites gives absorption bands in the region 580 - 700 nm. The absorption band in the range 320 - 375 nm corresponds to $^4A_2 \rightarrow {}^4T_1$. The absorption bands in the region 580 - 700 nm corresponds to $^4A_2 \rightarrow {}^4T_2$ [35]. Fig.7 (b) show the Tauc plots for y = 0.0 to y = 0.10 samples in the range 200 - 800 nm. The extrapolated band gaps (E_g) corresponds octahedral absorption bands are shown in Figs.8 and the values are given in Table 3. For y = 0.0, the band gap energy is 3.51 eV which is less compared with the band gap of $ZnAl_2O_4$ (3.8 eV) [36] which may be due to the quantum confinement limit [37]. It is observed that the E_g is decreased from 3.51 eV (y = 0.0) to 3.41 eV (y = 0.08) with Ce^{3+} doping, exhibit red shift. The red shift is caused by the *sp-d* interaction between band electrons and local electrons in the *d*-shell of the substituted cation and these interactions decreases the conduction band potential and increases the valence band potential, which leads to decrease in band gap [37].

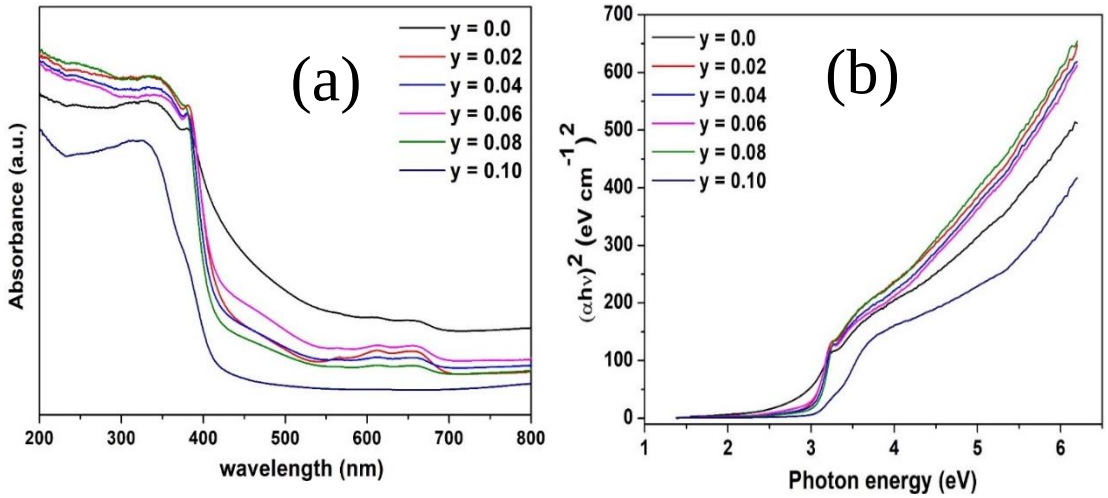

Fig.7 (a) UV-Vis absorbance spectra (b) Tauc plot for samples y = 0.0 – 0.10.

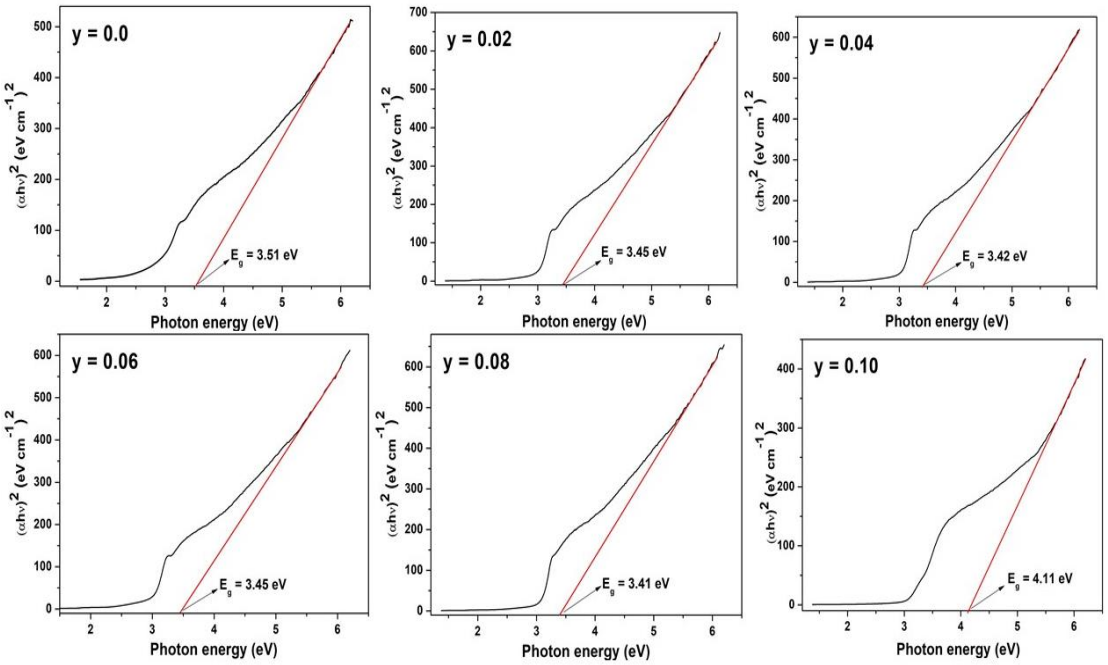

Fig.8 The Tauc plots for y = 0.0 - 0.10 samples.

Table 3. Optical energy band gap (E_g) for y = 0.0 - 0.10 samples.

y	(E_g, eV)
0.0	3.51
0.02	3.45
0.04	3.42
0.06	3.45
0.08	3.41
0.10	4.11

X-ray photoelectron spectroscopy (XPS):

Fig.9 (a) shows the X-ray photoelectron (XPS) wide spectra of $ZnAl_{2-x}Ce_xO_4$ (x = 0.06) sample. The X-ray photoelectron spectroscopy gives the information about the chemical composition and valence states of the elements. Fig. 9(b) shows the Ce 3d core level spectra for x = 0.06. The Ce 3d core spectra in Fig.9 (b) shows four intensity peaks at 881.02 eV (Ce^{4+}), 886.17 eV (Ce^{3+}) corresponds to Ce $3d_{5/2}$ and 901.30 eV (Ce^{4+}) and 905.80 eV (Ce^{3+}) assigned to Ce $3d_{3/2}$. Fig.9 (c) shows the core spectrum of Zn 2p. The two characteristic peaks at binding energies 1045.15 eV and 1022.04 eV are assigned to Zn $2p_{1/2}$ and Zn $2p_{3/2}$, respectively along with two satellite peak at 1012.80 eV and 1041.978 eV. The energy separation between Zn $2p_{3/2}$ and Zn $2p_{1/2}$ is 23.11 eV which confirms the presence of Zn^{2+} in all the samples. The presence of Zn $2p_{3/2}$ and Zn $2p_{1/2}$ clearly indicate that zinc with 2+ chemical state is occupying octahedral and tetrahedral sites in the crystal lattice, respectively. The core level XPS spectra of Al 2p for sample y = 0.06 is shown in Fig.9 (d).The binding energy is observed at 74.11 eV confirms the presence of Al^{3+} in y = 0.06. The peak observed at 530.81 eV is shown in Fig. 10(e), which indicates the bonding of oxygen with surrounding cations [38].

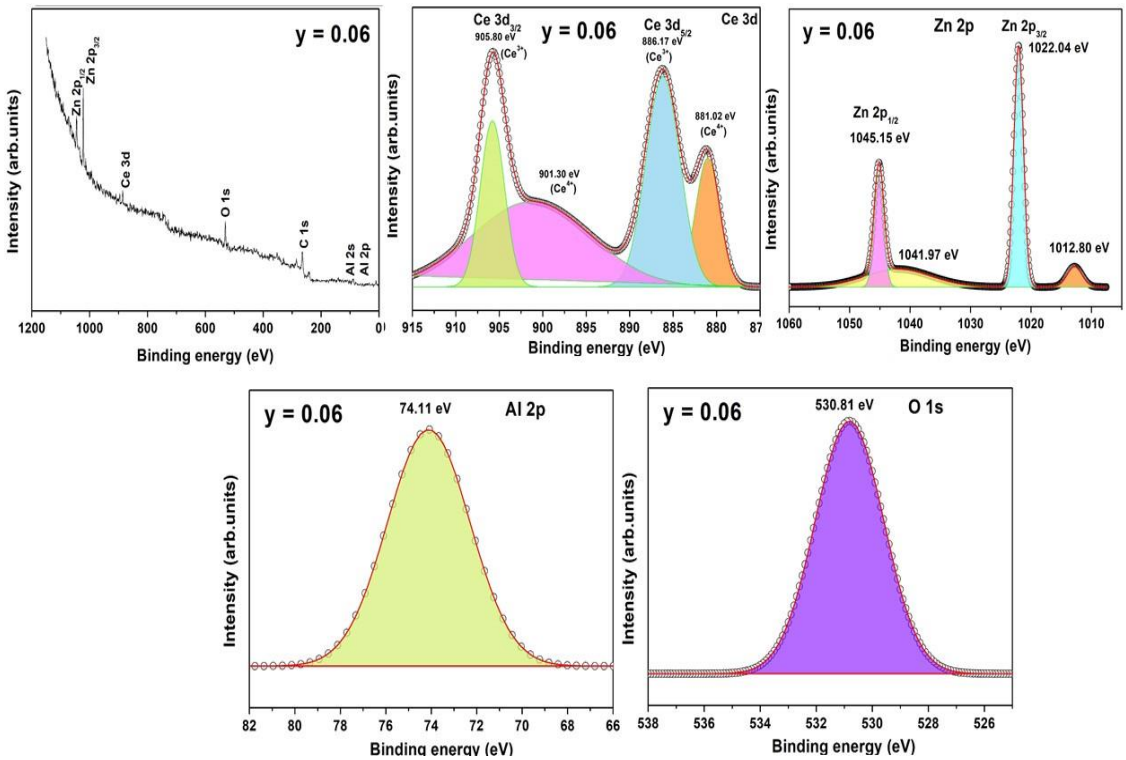

Fig.9 (a) X-ray photoelectron wide spectra of $ZnAl_{2-x}Ce_xO_4$ (x = 0.06). (b - e) Core level spectrum of Ce 3d, Zn 2p, Al 2p and O1s, respectively.

IV. Conclusion

The cerium doped $ZnAl_2O_4$ spinel were prepared by microwave hydrothermal method. It is observed that the lattice constant a is linearly increased from 8.085 Å (y = 0.0) to 8.404 Å (y = 0.10). It shows that with Ce doped $ZnAl_2O_4$ sample does obey Vegard's law. The FESEM images show irregular morphology and non-distribution of grains. The EDS spectrum of all the samples where the presence of Zn, Al, Ce, and O elements were confirmed. The structural bonds were assigned in FTIR. The prepared samples optical bandgap is determined by UV-Visible, the E_g is decreased from 3.51 eV (y = 0.0) to 3.41 eV (y = 0.08) with Ce^{3+} doping, exhibit red shift. With an optical band gap of this compounds can be used for ultraviolet (UV) photoelectronic devices. The X-ray

photoelectron spectroscopy gives the information about the chemical composition and valence states of the elements.

References

[1]. N.J. Van Der Laag, M.D. Snel, P.C.M.M. Magusin, G. De With, J. Eur. Ceram. Soc. 24 (2004) 2417.
[2]. G. Baldinozzi, D. Simeone, D. Gosset, S. Surble, L. Mazerolles, L. Thome, Nuclear Instrum. Methods Phys. Res. B 266 (2008) 2848.
[3]. Z. Lou, J. Hao, Appl. Phys. A 80 (2005) 151.
[4]. P. Latha, K. Prakash, S. Karuthapandian, Adv. Powder Technol. 28 (2017) 2903.
[5]. R. Ma, S. Zhanga, T. Wen, P. Gu, L. Li, G. Zhao, F. Niu, Q. Huang, Z. Tang, X. Wang, Catal. Today 335 (2019) 20.
[6]. Y.-C. Wu, D.-Y. Wang, T.-M. Chen, C.-S. Lee, K.-J. Chen, H.-C. Kuo, ACS Appl. Mater. Interfaces, 3 (2011) 3195.
[7]. Y. Li, J. Ding, Q. Wu, Q. Long, X. Wang, Y.Wang, J. Mater. Chem. C, 3 (2015) 8949.
[8]. I. Mindru, D. Gingasu, L. Patron, G. Marinescu, J.M. Calderon-Moreno, L. Diamandescu, M. Secu, O. Oprea, Mater. Res. Bull. 85 (2017) 240.
[9]. Samvit G. Menon, Deepak N. Hebbar, Suresh D. Kulkarni, K.S. Choudhari, C. Santhosh, Mater. Res. Bullet. 86 (2017) 63.
[10]. S.K.Sampath And J.F.Cordaro, J. Am. Ceram. Soc. 81 (1998) 649.
[11]. H.Matsui, C.N.Xu, H.Tateyama, Appl. Phys. Lett. 78 (2001)1068.
[12]. M.Zawadzki, Solid State Sci. 8 (2006) 14.
[13]. C.C.Yang, S.Y.Chen, S.Y.Cheng, Powder Technol. 148 (2004) 3.
[14]. X.Duan, D.Yuan, X.Wang, H.Xu, J. Sol-Gel Sci. Technol. 35 (2005) 221.
[15]. X.Duan, D.Yuan, Z.Sun, C.Luan, D.Pan, D.Xu, M.Lv, J. Alloys Comp. 386 (2005) 311.
[16]. N. Basavaraju, K.R. Priolkar, D. Gourier, S.K. Sharma, A. Bessière, B. Viana, Phys. Chem. Chem. Phys. 17 (2015) 1790.
[17]. K.C. Patil, M.S. Hegde, T. Rattan, S.T. Aruna, World Sci. 14 (2008) 75.
[18]. Katlakunta, Sadhana, Meena, Sher Singh, S. Srinath, M. Bououdina, R. Sandhya, K. Praveena, Mater.Res.Bullet. 63 (2015) 58.
[19]. K. Sadhana, K. Praveena, S.R. Murthy, J. Magn. Magn. Mater. 322 (2010) 3729.
[20]. I.H. Gul, F. Amin, A.Z. Abbasi, M.A. Rehman, A. Maqsood, Scr. Mater. 56 (2007) 497.
[21]. M.E. Rabanal, A. Varez, B. Levenfeld, J.M. Torralba, J. Mater. Process. Technol. 143 (2003) 470.
[22]. R.D. Shannon, Acta Crystallogr. 32 (1976) 751.
[23]. B.S. Ravikumar, H. Nagabhushana, S.C. Sharma, B.M. Nagabhushana, Spectrochimica Acta Part A: Molecular And Biomolecular Spectroscopy 122 (2014) 489.
[24]. V. Rathod, A.V. Anupama, R. Vijaya Kumar, V.M. Jali, B. Sahoo, Vib.Spectr, 92 (2017) 267.
[25]. A.A. Javidparvar, B. Ramezanzadeh, E.Ghasemi, Corrosion 72 (2016) 761.
[26]. S.V.Motloun, M.Tsega, L.F.Kpap, M.J. Hato, J.Alloys.Compd, 677 (2016) 72.
[27]. D.L. Ge, Y.J. Fan, C.L. Qi, Z.X. Sun, J. Mater. Chem. A, 1 (2013) 1651.
[28]. S. Mathur, M. Veith, M. Haas, H. Shen, N. Lecerf, V. Huch, S. Hüfner, H.P. Beck, M. Jilavi, J. Am. Ceram. Soc., 84 (2010) 1921.
[29]. P. Mcmillan, B. Piriou, J. Non-Cryst. Solids 53 (1982) 279.
[30]. J. Preudhomme, P. Tarte, Spectrochim. Acta Part A Mol. Spectrosc. 27 (1971) 1817.
[31]. D. Mazza, M. Vallino, G. Busca, J. Am. Ceram. Soc. 75 (1992) 1929.
[32]. H.R.Hoffmann, S.T. Martin, W. Choi, D.W. Bahnemann, Chem. Rev. 95 (1995) 69.
[33]. A.K.Singh, U. Nakate, Adv. Nanopart. 2 (2013) 66.
[34]. N. Pailhe, A. Wattiaux, M. Gaudon, A.J. Demourgues, Solid State Chem. 181 (2008) 1040.
[35]. W. Nie, F. M. Michel-Calendini, C. Linares, G. Boulon, C. Daul J.Luminescence 46 (1990) 177.
[36]. S.K. Sampath, D.G. Kanhere, R. Pandey, J. Phys. Condens. Matter 11 (1999) 3635.
[37]. Huang Shang-Pan, Wei Zhi-Qiang, Wu Xiao-Juan, Shi Ji-Wen, Mater. Res.Exp. 7(1) (2020) 015025.
[38]. B.R. Strohmeier, Surf. Sci. Spectra 3(1995) 129.